Scripta Materialia 190 (2021) 46–51

Contents lists available at ScienceDirect

Scripta Materialia

journal homepage: www.elsevier.com/locate/scriptamat

Additive manufacturing of three-dimensional (3D)-architected CoCrFeNiMn high- entropy alloy with great energy absorption

Siyuan Peng[a,b], Shahryar Mooraj[a], Rui Feng[c], Liang Liu[a], Jie Ren[a], Yanfang Liu[a], Fanyue Kong[a], Zhiyu Xiao[b], Cheng Zhu[d], Peter K. Liaw[c], Wen Chen[a,*]

[a] Department of Mechanical and Industrial Engineering, University of Massachusetts, Amherst, MA 01003-2210, USA
[b] National Engineering Research Center of Near-Net-Shape Forming for Metallic Materials, South China University of Technology, Guangzhou 510640, People's Republic of China.
[c] Department of Materials Science and Engineering, The University of Tennessee, Knoxville, TN 37996, USA
[d] Lawrence Livermore National Laboratory, Livermore, CA 94550, USA

ARTICLE INFO

Article history:
Received 5 June 2020
Revised 3 August 2020
Accepted 19 August 2020
Available online 28 August 2020

Keywords:
Additive manufacturing
Direct ink writing
High-entropy alloy
Architected materials
Mechanical property

ABSTRACT

In this study, we developed an approach to additive manufacturing of three-dimensional (3D)-architected CoCrFeNiMn high-entropy alloys by direct ink writing combined with thermal sintering. The 3D-architected CoCrFeNiMn lattices exhibit the outstanding energy absorption capacity that expands the envelope of existing architected materials. Such a high-energy absorption ability originates from the bend-dominated deformation mode of the 3D-architecture as well as the fully-annealed homogeneous microstructure of equiaxed grains, which collectively lead to remarkable strain hardening upon deformation. Our study provides a new avenue for 3D-printing advanced architected materials with extreme mechanical energy absorption for a myriad of structural applications.

Architected materials are ubiquitous in nature and engineering materials alike. For example, wood and bone are biologically-architected materials with low weight and superior mechanical properties [1]. Architected materials are often desirable for a wide variety of engineering applications, such as heat exchange [2], catalysis [3,4], mechanical damping, and energy absorption [5–9]. The performance of architected materials is governed by their topology and the constituent material. Conventional manufacturing techniques for architected materials often rely on joining and foaming of the liquid melt, which impose a limitation on the topology [10]. With the recent advancement of additive manufacturing (AM), also called three-dimensional (3D) printing technologies, materials and components with 3D geometrically-complex topologies that were previously difficult can now be directly realized [5,6,8]. Through AM, architected materials have been thus far synthesized in many engineering materials, such as steels [11], titanium alloys [12], aluminum alloys [13], or even ceramics [14].

A material class in which the development of architected materials towards superior mechanical performance is promising is high-entropy alloys (HEAs). HEAs are a new family of materials that contain high concentrations of five or more different elements in near equi-atomic proportions [15–17]. They are different from the conventional alloys that usually consist of one primary element with low concentrations of other alloying elements. Conceptually, this radical departure from the conventional alloy-design motif opens up a new avenue for explorations of new materials. Although some fundamental understanding, such as the thermodynamic origin of the phase selection of HEAs, remains elusive, HEAs have been reported to exhibit exceptional mechanical properties, including ultrahigh fracture toughness paired with comparable strength to that of some metallic glasses, making them promising candidates for engineering applications [15,18–20]. To harness the combined advantages of AM and HEAs, significant efforts on AM of HEAs have been made in recent years [21–28]. Earlier studies mainly focused on laser- or electron-based AM methods, including selective laser melting (SLM) [26], laser engineering net shaping (LENS) [29,30], and electron beam melting (EBM) [31]. However, these methods have some inherent limitations, such as the intensive energy requirement and high operation costs [32]. The highly-localized melting, strong temperature gradient, and great solidification-front velocity associated with these AM processes generate extremely nonequilibrium microstructures associated with complex thermal histories that often result in sig-

* Corresponding author.
E-mail address: wenchen@umass.edu (W. Chen).

https://doi.org/10.1016/j.scriptamat.2020.08.028
1359-6462/

nificant residual stresses or even micro-cracks that deteriorate the performance and fidelity of the fabricated parts or architectures [33,34].

To overcome these limitations, Kenel et al. [35] recently introduced a novel AM approach to fabricate a 3D CoCrFeNi HEA architected microlattices by direct ink writing (DIW) combined with thermal sintering. DIW is an emerging low-cost 3D-extrusion-based AM technique that enables 3D printing of materials into complex architectures with high fidelity [36–39]. The CoCrFeNi HEA microlattices was synthesized by DIW of colloidal inks containing a blend of oxide nano-powders (Cr_2O_3, NiO, Fe_2O_3, Co_3O_4), followed by co-reduction and sintering of the oxide inks into a solid-solution alloy in a flowing hydrogen (H_2) environment. The sintered CoCrFeNi microlattices exhibit outstanding mechanical properties at cryogenic and ambient temperatures [35]. Despite the blend of a variety of oxide nano-powder inks enables some compositional flexibility in printing HEAs, the requirement of co-reduction sintering poses an inherent challenge in fabricating HEAs containing reactive constituent elements, such as Al, Mg, Ti, Mn, the oxides of which (i.e., Al_2O_3, MgO, TiO, and MnO) are all difficult to be reduced by H_2 based on the well-known Ellingham diagram [40]. Nevertheless, these reactive elements are often designed as critical constituent elements in HEAs to achieve desired mechanical and physical performance [41]. Here, using CoCrFeNiMn as an example, we develop an approach to AM of 3D-architected HEAs by DIW of pre-alloyed CoCrFeNiMn micro-powders combined with direct post-sintering. The sintered 3D-architected CoCrFeNiMn demonstrates a homogeneous microstructure with exceptional mechanical energy absorption that far exceeds conventional metal architectures.

Within the DIW process, structures are built layer-by-layer through the filamentary deposition of inks. A critical step of this AM technology is the development of inks with appropriate rheological properties so that they can flow through a micro-nozzle to form continuous filaments under pressure and drying upon exiting to retain their shape (Fig. 1a). In this study, we developed an ink formulation comprised of organic solvents of 10 mL Tetrahydrofuran (THF, Fisher Scientific) and 0.1 mL 2-Butoxyethanol (Fisher Scientific), 1 gram Poly(methyl methacrylate) - poly(n-butyl acrylate), i.e., PMMA-PnBA block co-polymer binder (Kuraray American, Inc.), and 32 grams pre-alloyed CoCrFeNiMn micro-powders by gas atomization (size: 15 ~ 32 μm, Jiangsu VILORY New Material Technology Co, Ltd. China). A volumetric ratio of 8:2 was adopted for the CoCrFeNiMn micro-powders and the binding polymer, respectively, for the ink synthesis. To ensure homogeneity, the ink was mixed by a planetary centrifugal mixter (Thinky Are-310). After stabilization, the ink showed a typical shear-thinning characteristic with a shear viscosity range of 10^2 - 10^5 Pa•s that is appropriate for DIW (Fig. 1b). The ink was thereafter loaded into a syringe-barrel (Nordson EFD) and pressurized through a tapered nozzle of 250 μm in diameter onto a planar alumina substrate under a computer digital control. To achieve the 3D-architected CoCrFeNiMn, exemplary woodpile lattices of different relative densities were printed by adjusting the spacing (or the so-called hatch distance) of the filaments ranging from 250 μm to 800 μm while maintaining the filament diameter of ~ 250 μm (Fig. 1c). Each subsequent layer was rotated by 90° from the previous layer and no shift between layers was used for all the microlattices. The printed CoCrFeNiMn lattices were sintered in a tube furnace (KSL-1700X-KS, MTI) under the flowing Argon (99.99 wt%, 200 ml/min, Airgas). A multi-step heating profile with a heating rate of 5 K/min. was used to remove the moisture (373 K, 0.5 hr), organic solvents (500 K, 1 hr), and binding polymer (700 K, 1hr), followed by thermal sintering at the peak temperature (1,420 K, 12 hrs) and eventually furnace cooled (Fig. 1d). Note that such a peak sintering temperature was selected as approximately 0.95 T_m, where the equilibrium melting temperature, $T_m \approx$ 1,530 K, for the CoCrFeNiMn alloy [42]. The average linear shrinkage of the CoCrFeNiMn sample after sintering is approximately 12.3%. The shrinkage results from the evaporation of the excess solvents, the burnout of the polymer binder, and the solid-state-sintering-induced volume reduction. In comparison with prior studies, the linear shrinkage of our CoCrFeNiMn is similar to the sintered Ni-Mn-Ga (10-15%) [43]. In other examples of metal lattices fabricated by direct ink writing of metal oxides combined with hydrogen co-reduction sintering, the linear shrinkages are significantly higher, for example, 44% for Fe (sintered from Fe_2O_3) [44], 40% for Ni (sintered from NiO) [44], and 45% for CoCeFeNi (sintered from a mixture of Co_3O_4, Cr_2O_3, Fe_2O_3, and NiO powders) [35]. These higher shrinkages possibly arise from the oxygen loss during the hydrogen reduction process [44].

Microstructural analysis was conducted by a scanning electron microscope (SEM, Zeiss EVO) equipped with a Bruker's QUANTAX e-Flash electron backscatter diffraction (EBSD) detector. The crystal structure of the sintered sample was confirmed by Panalytical X-ray diffraction (XRD), using a Cu-K_α target with the 2θ scanning range of 20° ~ 100° at a scanning rate of 8°/min. The chemical compositions of the prealloyed powders and the sintered samples were measured by the inductively-coupled plasma mass spectrometry (ICP-MS) and SEM-EDX (energy-dispersive X-ray spectroscopy), respectively. The relative density of the sintered microlattices was measured by the weight and geometric volume. To study the energy absorption of the 3D-architected CoCrFeNiMn, uniaxial compression tests of the microlattices with dimensions of approximately 5 mm × 5 mm × 4 mm (height) were performed on an Instron 5969 machine with a strain rate of 5×10^{-4} s^{-1} at room temperature. The displacement and the strain were precisely recorded by a non-contact AVE2 video extensometer. To facilitate the fundamental understanding of the microstructure and the mechanical property of the constituent material of the 3D-architected CoCrFeNiMn, bulk specimens were also printed and sintered under the same processing conditions. Bulk uniaxial compression pillars of 2 mm × 2 mm × 4 mm (height) were cut by electrical discharge machining and tested under the same strain rate.

Fig. 2 shows the SEM image, XRD pattern, EBSD inverse pole figure (IPF) of the 3D-architected CoCrFeNiMn in both the as-sintered state and deformed states at compressive strains of 15% and 45%. The microstructural evolution after deformation is shown here for a direct comparison and will be discussed later. In the as-sintered state, a homogeneous single-phase FCC structure was revealed (Figs. 2a-d). The SEM-EDX revealed a similar chemical composition of the sintered specimen, as compared to the prealloyed powders, of which the composition was measured by ICP-MS (Table S1). Moreover, a highly-uniform elemental distribution was identified after sintering (Fig. S1). The EBSD-IPF map (Fig. 2d) shows the prevalence of the equiaxed coarse grain structure with randomly-oriented grains. The grain size ranges from a few microns to 50 microns, with an average grain size of approximately 24.3 μm (Fig. S2). Meanwhile, annealing twins were frequently observed in the grain interior, which has also been reported in the sintered CoCrFeNi HEA [35] and in fully-recrystallized CoCrFeNiMn HEAs [15]. Overall, this well-annealed equiaxed microstructure is fundamentally distinct from that prepared by the other energy intensive laser or electron beam-based AM, whereby far-from-equilibrium microstructures often prevail [45]. This trend suggests that the DIW technique has the potential to provide structurally-homogenous samples with negligible residual stresses due to the full inter-diffusion and isothermal sintering [35]. Nevertheless, some residual pores of ~ 5% by the volume fraction (estimated by the ImageJ software) were also observed, mainly located at grain boundaries and triple junctions (Fig. 2d), despite the relatively-high sintering temperature ($0.95T_m$) and long sin-

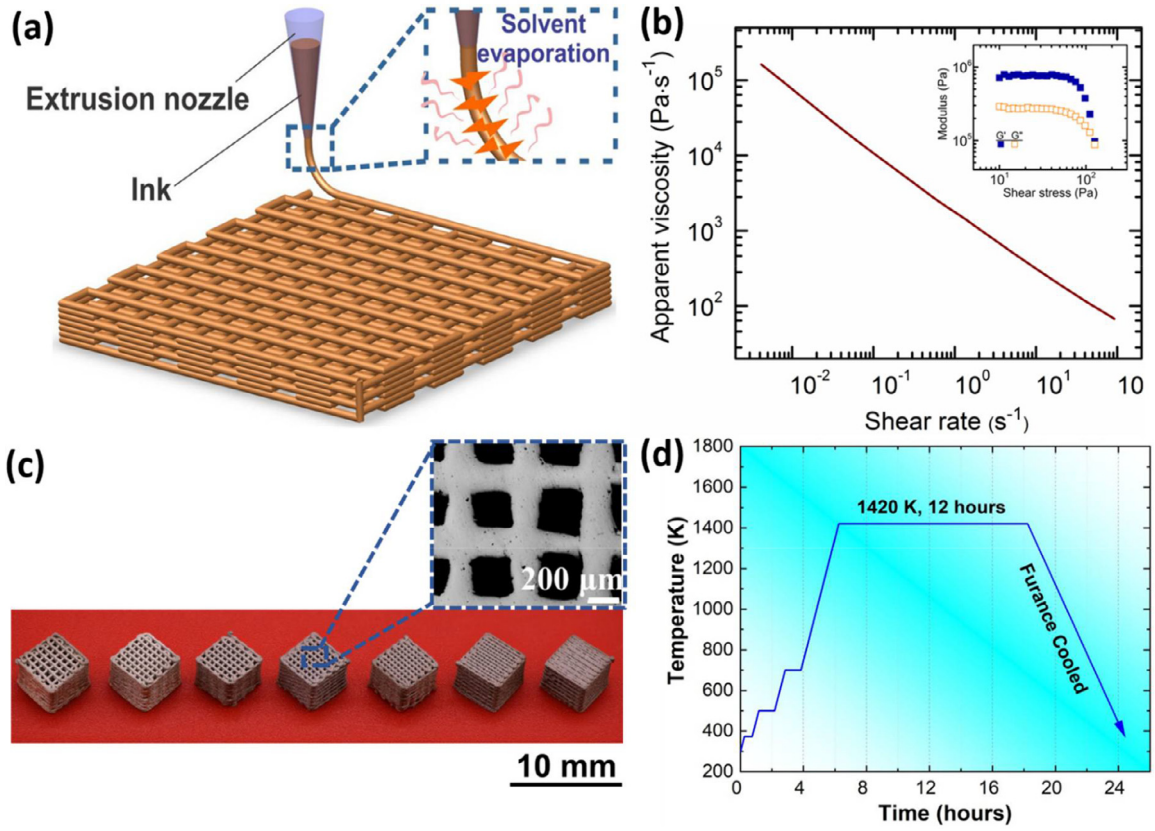

Fig. 1. Fabrication process of the 3D-architected CoCrFeNiMn. (a) Schematic illustration of the DIW technique. During the DIW process, a suspension ink is extruded through a nozzle to print the desired 3D-architected materials. The inset image shows the rapid solvent evaporation after extrusion. (b) Rheological properties of the CoCrFeNiMn ink. The apparent viscosity continuously decreases with increasing the shear rate, resulting in a shear-thinning viscoelastic behavior. The storage modulus (G') and the loss modulus (G") are sensitive to the varying shear stresses (or strains) and form a "crossover", which is necessary for printability, suggesting a liquid-like behavior during DIW and a solid-like behavior after printing to facilitate shape retention. (c) Photograph of the CoCrFeNiMn woodpile lattices with gradually increasing relative densities after sintering by continuously decreasing filament spacing from left to right. (d) A multi-step sintering process of the 3D-architected CoCrFeNiMn.

tering time (12 hrs). Compared with the sintered CoCrFeNi HEA by co-reduction sintering that shows a low porosity of ~ 0.4% [35], the significant residual pores here may be attributed to the large starting powder sizes of 15 ~ 32 μm that result in a less driving force at the last stage (i.e., densification) of solid-state sintering [46].

A typical compressive engineering stress-strain (σ-ε) curve of the 3D-architected HEA is shown in Fig. 3a. Similar to many other ductile architected materials [1], the σ-ε curve of the 3D-architected CoCrFeNiMn is characterized by three progressive deformation stages: (i) linear elasticity; (ii) plastic flow plateau; and (iii) final densification. The flow stress smoothly increases with no stress serrations and exhibits the pronounced strain-hardening characteristic in the plastic-plateau stage, suggesting that the struts of the 3D-architected CoCrFeNiMn lattice are plastically deforming rather than fracturing upon compression [47]. The densification stage is designated by a rapid stress rise after the plateau stage. The densification strain, ε_{d0}, can be quantitatively determined by an energy-absorption-efficiency method, which yields a precise and consistent measure for the onset of the densification [48,49].

Fig. 3b shows the σ-ε curves of the 3D-architected CoCrFeNiMn lattices with a wide range of relative densities from 0.35 to 0.69. The σ-ε curve of the bulk specimen under the same sintering protocol is shown in Fig. S3 (Supplementary Materials). The yield strength (0.2% proof stress) of the HEA lattices scales directly with the relative density. In general, the Gibson-Ashby model can be well adopted to quantify the yield-stress dependence of an open-cell architected material on the relative density as follows [1]:

$$\frac{\sigma^*}{\sigma_s} \propto \left(\frac{\rho^*}{\rho_s}\right)^n \tag{1}$$

where $\sigma_s \approx 196$ MPa is the yield strength of the bulk constituent CoCrFeNiMn alloy (Fig. S3). ρ_s is the density of the bulk sample. σ^* and ρ^* are the yield strength and the density of the 3D-architected CoCrFeNiMn lattices, respectively. The value of the scaling exponent, n, depends on the nature of the deformation mode in the material: $n \approx 1$ when the struts deform under axial stresses (stretch-dominated), and $n \approx 2$ ~ 3 when the struts deform under bending stresses (bend-dominated) [1]. Here, by plotting the relative yield strength, σ^*/σ_s, as a function of the relative density, ρ^*/ρ_s, on a logarithmic scale (Fig. 3c), $n \approx 1.9$ was fitted, suggesting a bend-dominated deformation mechanism in the 3D-architected HEA woodpile lattices.

Among the mechanical properties of architected materials, the energy absorption per unit volume upon densification (W) is critical for their structural applications [1]. W is quantitatively described by

$$W = \int_0^{\varepsilon_{d0}} \sigma(\varepsilon) d\varepsilon \tag{2}$$

where the onset of densification strain, ε_{d0}, is the strain at the maximum energy-absorption efficiency. The energy-absorption ef-

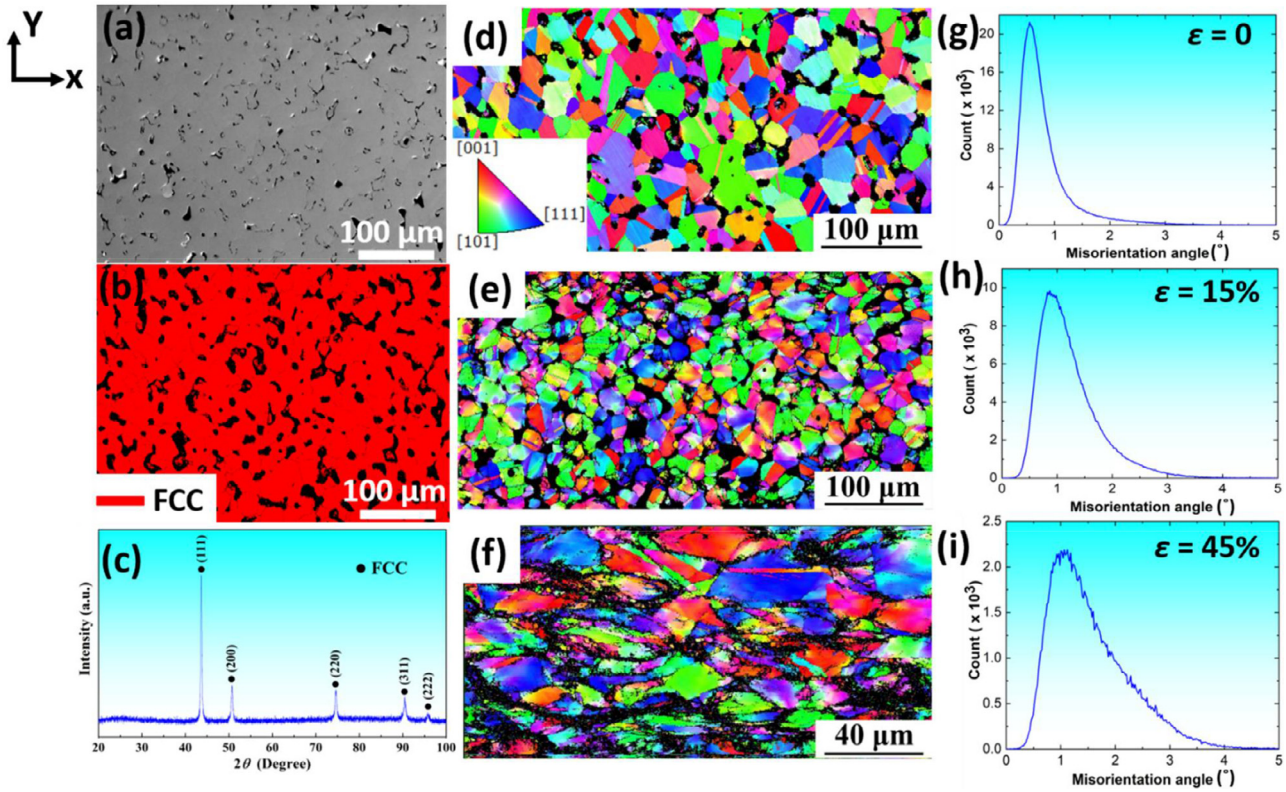

Fig. 2. Microstructural characterization of the 3D-architected CoCrFeNiMn. (a) SEM image. (b) EBSD-phase map of the same area of (a). Note the areas nearby the micropores were difficult to be indexed. (c) XRD pattern. (d)-(f) EBSD-IPF images of the 3D-architected CoCrFeNiMn in the as-sintered state, deformed at strains of 15% and 45%, respectively. (g)-(i) statistical kernel average misorientation (KAM) angle distribution at different strain stages (refer to Fig. S5 for the KAM images). Note that the compression is along the Y-direction and the IPF map is along the X-direction.

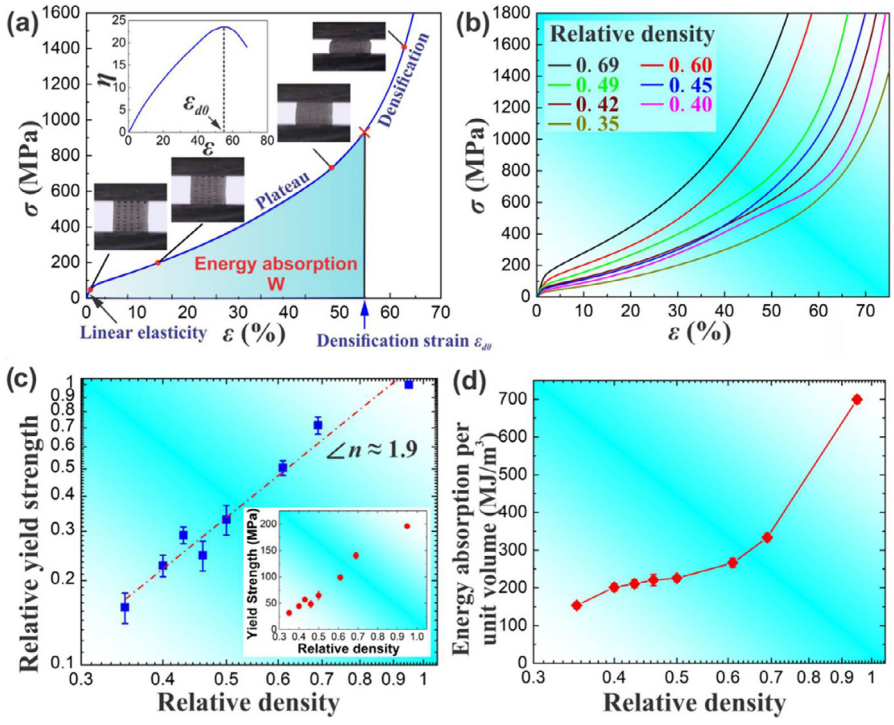

Fig. 3. Mechanical properties of 3D-architected CoCrFeNiMn lattices. (a) Representative compressive stress-strain (σ-ε) curve. Three deformation stages of (i) linear elasticity, (ii) plastic plateau, and (iii) final densification are identified. The progressive deformation morphologies of the 3D-architected lattice are in-situ captured by a camera (b) Compressive σ-ε curves of the 3D-architected CoCrFeNiMn woodpile lattices with different relative densities ranging from 0.35 to 0.69. (c) Scaling plot of the relative yield stress (σ^*/σ_s) versus relative density, ρ^*/ρ_s. (d) Plot of energy absorption per unit volume (W) versus relative density. The mechanical properties of the sintered bulk CoCrFeNiMn (Fig. S3) are included in (c) and (d).

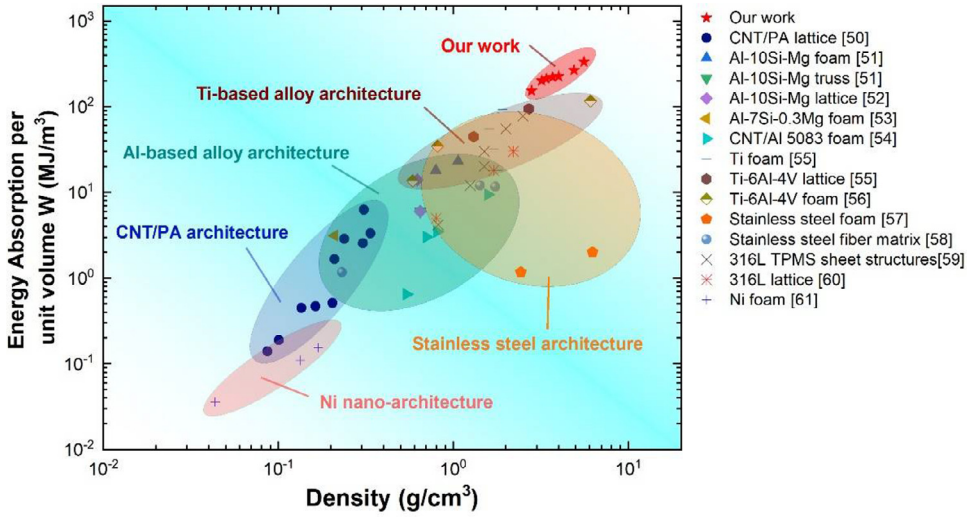

Fig. 4. Ashby chart of energy absorption per unit volume versus density of the 3D-architected CoCrFeNiMn lattices in direct comparison with existing advanced metallic and composite-architected materials. Both stochastic foams and 3D-printed periodic lattices are included here.

ficiency, η, is strain-dependent and is defined by [49]

$$\eta(\varepsilon) = \frac{1}{\sigma(\varepsilon)} \int_0^{\varepsilon} \sigma(\varepsilon) d\varepsilon \tag{3}$$

Therefore, ε_{d0} can be simply identified by the differentiation of Eq. (3)

$$\left.\frac{d\eta(\varepsilon)}{d\varepsilon}\right|_{\varepsilon=\varepsilon_{d0}} = 0 \tag{4}$$

A typical η–ε curve is shown in the Fig. 3a inset whereby ε_{d0} is denoted. Combining Eqs. (2)-(4), the energy absorption per unit volume versus relative density was calculated and plotted in Fig. 3d. Notably, W continuously increases from 155 to 333 MJ/m^3 as the relative density of the 3D-architected CoCrFeNiMn lattice increases from 0.35 to 0.69. This trend is consistent with the strong dependence of the flow stress on the relative density (Fig. 3b). For a direct comparison with architected structures made of other materials, an energy absorption-density Ashby chart is constructed (Fig. 4), in which the 3D-architected CoCrFeNiMn exhibits outstanding energy absorption that is not accessible by existing architected materials, such as steel and titanium alloy architectures with similar densities [50–61]. For example, when $\rho^* \approx 6$ g/cm^3, $W = 333$ MJ/m^3 for our AM 3D-architected CoCrFeNiMn, which is almost three times of $W = 116$ MJ/m^3 for the Ti-6Al-4V architected materials [56] and two orders of magnitude higher than that of $W \approx 2$ MJ/m^3 for the stainless-steel foams [57]. To further compare with the mechanical performance of the lightweight-architected materials, such as the aluminum-alloy foams or lattices, the specific energy-absorption capacity, $U = W/\rho^*$, is also employed here to normalize the density effect. The remarkable specific energy absorption of $U = 54$ ~ 63 J/g is derived for the 3D-architected CoCrFeNiMn, which rivals the mechanically-efficient Al-10Si-Mg (wt.%) gyroid lattices (20 ~ 25 J/g) [52], architected carbon nanotube (CNT)-polyamides (PA) composites with auxetic structures (~ 20 J/g) [50], and lightweight hollow nickel nano-lattices (~ 1 J/g) [2] (Fig. 4). Compared with the CoCrFeNi HEA microlattice with a grain size range of 35 ~ 80 μm, at the same relative density of ~ 60%, $\sigma^* \approx 90$ MPa, and $W = 235$ MJ/m^3 for the CoCrFeNiMn microlattice, which are slightly higher than 77 MPa and 210 MJ/m^3 for the CoCrFeNi microlattice [35] (Fig. S4).

We speculate that the outstanding energy absorption of the 3D-architected CoCrFeNiMn is attributed to the fully-annealed microstructure where remarkable strain-hardening was observed in both the 3D lattices and the constituent bulk specimen (Figs. 3 and S3). To understand the microscopic deformation mechanism, the deformed microstructures at different strain stages of 0% (as-sintered), 15%, and 45% were analyzed by EBSD (Figs. 2d-i and S5). The average grain size was drastically decreased from ~ 24 μm in the as-sintered state to ~ 10 μm at $\varepsilon = 45\%$ together with a noticeable increase in the local misorientation, suggesting the multiplication of geometrically-necessary dislocations (GNDs) upon deformation [62,63]. The density of GNDs, ρ_{GND}, can be quantitatively estimated, based on [64]

$$\rho_{GND} = \frac{2\theta_{KAM}}{xb} \tag{5}$$

where θ_{KAM} is the kernel average misorientation angle ($\theta_{KAM} \approx$ 0.0139, 0.0213, and 0.0268 for $\varepsilon = 0\%$, 15%, and 45%, respectively). x is the unit length, $x = 2 * Px$, which Px is the step size used in the EBSD acquisition. $b \approx 0.254$ nm is the Burgers vector (the lattice constant, $a = 0.3592$ nm was calculated from the XRD). Hence, $\rho_{GND} \approx 1.18 \times 10^{14}$ m^{-2}, 1.78×10^{14} m^{-2}, and 5.52×10^{14} m^{-2} for $\varepsilon = 0\%$, 15%, and 45%, respectively. In addition to such an intrinsic dislocation-hardening mechanism in the constituent material, the bend-dominated macroscopic deformation mode of the woodpile lattices is likely to be another mechanism responsible for the remarkable strain hardening of the 3D-architected CoCrFeNiMn upon compression, as evidenced in many other ductile-architected metals with a woodpile lattice topology [65].

In summary, we have developed an approach to AM of 3D-architected HEAs by DIW of the pre-alloyed CoCrFeNiMn combined with direct post-sintering. The 3D-architected CoCrFeNiMn woodpile lattices exhibit an exceptional energy-absorption capability that expands the envelope of existing architected materials. Such a high energy-absorption ability originates from the bend-dominated deformation mode of the architecture topology as well as the fully-annealed microstructure of homogeneous and equiaxed grains, which collectively result in significant strain hardening upon deformation. Our work offers new opportunities for designing and 3D-printing advanced architected materials with extreme mechanical energy absorption for many applications, including packaging and other highly-value-added industries. Further work will be performed in the future to fully understand the micro-mechanisms of the plastic deformation in these 3D-architected HEAs, which is essential towards the optimized microstructure and architecture topology.

Declaration of Competing Interest

The authors declare that they have no known competing financial interests or personal relationships that could have appeared to influence the work reported in this paper.

Acknowledgements

S.P. is grateful for visiting scholarships provided by the China Scholarship Council. W.C. conceived and supervised the project. S.P. and S.M. designed the ink and performed the direct ink writing, C.Z. characterized the rheology of the ink, under the auspices of the U.S. Department of Energy by Lawrence Livermore National Laboratory under Contract DE-AC52-07NA27344. IM release number: LLNL-JRNL-811202. S.P., R.F., P.L., J.R., L.L., F.K., and Y.L. carried out the microstructural characterization and mechanical testing, S.P. and W.C. drafted the initial manuscript. All authors contributed to the data analysis, discussion, and manuscript writing. P.L. very much appreciates the supports from the National Science Foundation (DMR-1611180 and 1809640) with the program directors, Drs. J. Yang, J. G. Shiflet, and D. Farkas.

Supplementary materials

Supplementary material associated with this article can be found, in the online version, at doi:10.1016/j.scriptamat.2020.08.028.

References

[1] L.J. Gibson, M.F. Ashby, Cellular Solids, Structure and Properties, Cambridge university press, 1999.
[2] N.G. Dou, R.A. Jagt, C.M. Portela, J.R. Greer, A.J. Minnich, Nano Lett. 18 (2018) 4755–4761.
[3] C. Zhu, Z. Qi, V.A. Beck, M. Luneau, J. Lattimer, W. Chen, M.A. Worsley, J. Ye, E.B. Duoss, C.M. Spadaccini, Sci. Adv. 4 (2018) eaas9459.
[4] E. Detsi, M. Van De Schootbrugge, S. Punzhin, P. Onck, J. De Hosson, Scr. Mater. 64 (2011) 319–322.
[5] X. Zheng, H. Lee, T.H. Weisgraber, M. Shusteff, J. DeOtte, E.B. Duoss, J.D. Kuntz, M.M. Biener, Q. Ge, J.A. Jackson, Science 344 (2014) 1373–1377.
[6] X. Zheng, W. Smith, J. Jackson, B. Moran, H. Cui, D. Chen, J. Ye, N. Fang, N. Rodriguez, T. Weisgraber, Nat. Mater. 15 (2016) 1100–1106.
[7] L.R. Meza, S. Das, J.R. Greer, Science 345 (2014) 1322–1326.
[8] W. Chen, S. Watts, J.A. Jackson, W.L. Smith, D.A. Tortorelli, C.M. Spadaccini, Sci. Adv. 5 (2019) eaaw1937.
[9] M.-S. Pham, C. Liu, I. Todd, J. Lertthanasarn, Nature 565 (2019) 305–311.
[10] A.G. Evans, J.W. Hutchinson, M.F. Ashby, Curr. Opin. Solid State Mater. Sci. 3 (1998) 288–303.
[11] L.-E. Rännar, A. Koptyug, J. Olsén, K. Saeidi, Z. Shen, Additive Manuf. 17 (2017) 106–112.
[12] X. Wang, S. Xu, S. Zhou, W. Xu, M. Leary, P. Choong, M. Qian, M. Brandt, Y.M. Xie, Biomaterials 83 (2016) 127–141.
[13] C. Yan, L. Hao, A. Hussein, S.L. Bubb, P. Young, D. Raymont, J. Mater. Process. Technol. 214 (2014) 856–864.
[14] Z.C. Eckel, C. Zhou, J.H. Martin, A.J. Jacobsen, W.B. Carter, T.A. Schaedler, Science 351 (2016) 58–62.
[15] B. Gludovatz, A. Hohenwarter, D. Catoor, E.H. Chang, E.P. George, R.O. Ritchie, Science 345 (2014) 1153–1158.
[16] Y. Ye, Q. Wang, J. Lu, C. Liu, Y. Yang, Mater. Today 19 (2016) 349–362.
[17] J. Yeh, S. Chen, S. Lin, J. Gan, T. Chin, T. Shun, C. Tsau, S. Chang, Adv. Eng. Mater. 6 (2004) 299–303.
[18] B. Gludovatz, E.P. George, R.O. Ritchie, Jom 67 (2015) 2262–2270.
[19] Y. Zhang, T.T. Zuo, Z. Tang, M.C. Gao, K.A. Dahmen, P.K. Liaw, Z.P. Lu, Prog. Mater Sci. 61 (2014) 1–93.
[20] D.B. Miracle, J.D. Miller, O.N. Senkov, C. Woodward, M.D. Uchic, J. Tiley, Entropy 16 (2014) 494–525.
[21] Z. Zhu, Q. Nguyen, F. Ng, X. An, X. Liao, P. Liaw, S. Nai, J. Wei, Scr. Mater. 154 (2018) 20–24.
[22] V. Ocelík, N. Janssen, S. Smith, J.T.M. De Hosson, Jom 68 (2016) 1810–1818.
[23] M. Li, J. Gazquez, A. Borisevich, R. Mishra, K.M. Flores, Intermetallics 95 (2018) 110–118.
[24] J. Joseph, T. Jarvis, X. Wu, N. Stanford, P. Hodgson, D.M. Fabijanic, Mater. Sci. Eng.: A 633 (2015) 184–193.
[25] T. Fujieda, H. Shiratori, K. Kuwabara, T. Kato, K. Yamanaka, Y. Koizumi, A. Chiba, Mater. Lett. 159 (2015) 12–15.
[26] Y. Brif, M. Thomas, I. Todd, Scr. Mater. 99 (2015) 93–96.
[27] X. Li, Adv. Eng. Mater. 20 (2018) 1700874.
[28] S. Gorsse, C. Hutchinson, M. Gouné, R. Banerjee, Sci. Technol. Adv. Mater. 18 (2017) 584–610.
[29] X. Gao, Y. Lu, Mater. Lett. 236 (2019) 77–80.
[30] Y. Chew, G.J. Bi, Z.G. Zhu, F.L. Ng, F. Weng, S.B. Liu, S.M.L. Nai, B.Y. Lee, Mater. Sci. Eng.: A 744 (2019) 137–144.
[31] K. Kuwabara, H. Shiratori, T. Fujieda, K. Yamanaka, Y. Koizumi, A. Chiba, Additive Manuf. 23 (2018) 264–271.
[32] W.E. Frazier, J. Mater. Eng. Perform. 23 (2014) 1917–1928.
[33] A.S. Wu, D.W. Brown, M. Kumar, G.F. Gallegos, W.E. King, Metall. Mater. Trans. A 45 (2014) 6260–6270.
[34] W. Chen, T. Voisin, Y. Zhang, J.-B. Florien, C.M. Spadaccini, D.L. McDowell, T. Zhu, Y.M. Wang, Nat. Commun. 10 (2019) 1–12.
[35] C. Kenel, N.P. Casati, D.C. Dunand, Nat. Commun. 10 (2019) 1–8.
[36] J.E. Smay, J. Cesarano, J.A. Lewis, Langmuir 18 (2002) 5429–5437.
[37] M. Young, R. Rao, J. Almer, D. Haeffner, J. Lewis, D.C. Dunand, Acta Mater. 57 (2009) 2362–2375.
[38] S. Mooraj, S.S. Welborn, S. Jiang, S. Peng, J. Fu, S. Baker, E.B. Duoss, C. Zhu, E. Detsi, W. Chen, Scr. Mater. 177 (2020) 146–150.
[39] W. Chen, L. Thornley, H.G. Coe, S.J. Tonneslan, J.J. Vericella, C. Zhu, E.B. Duoss, R.M. Hunt, M.J. Wight, D. Apelian, Appl. Phys. Lett. 110 (2017) 094104.
[40] M. Hasegawa, in: in: Treatise on Process Metallurgy, Elsevier, 2014, pp. 507–516.
[41] X. Fu, C.A. Schuh, E.A. Olivetti, Scr. Mater. 138 (2017) 145–150.
[42] B. Wang, A. Fu, X. Huang, B. Liu, Y. Liu, Z. Li, X. Zan, J. Materi Eng. Perform. 25 (2016) 2985–2992.
[43] S.L. Taylor, R.N. Shah, D.C. Dunand, Acta Mater. 143 (2018) 20–29.
[44] S.L. Taylor, A.E. Jakus, R.N. Shah, D.C. Dunand, Adv. Eng. Mater. 19 (2017) 1600365.
[45] R. Li, P. Niu, T. Yuan, P. Cao, C. Chen, K. Zhou, J. Alloys Compd. 746 (2018) 125–134.
[46] Z.Z. Fang, Sintering of Advanced Materials, Elsevier, 2010.
[47] E. Hong, B.Y. Ahn, D. Shoji, J.A. Lewis, D.C. Dunand, Adv. Eng. Mater. 13 (2011) 1122–1127.
[48] Y. Sun, B. Amirrasouli, S. Razavi, Q. Li, T. Lowe, P. Withers, Acta Mater. 110 (2016) 161–174.
[49] M. Avalle, G. Belingardi, R. Montanini, Int. J. Impact Eng. 25 (2001) 455–472.
[50] S. Yuan, C.K. Chua, K. Zhou, Adv. Mater. Technol. 4 (2019) 1800419.
[51] I.N. Orbulov, A. Szlancsik, Adv. Eng. Mater. 20 (2018) 1700980.
[52] I. Maskery, N.T. Aboulkhair, A.O. Aremu, C.J. Tuck, I.A. Ashcroft, R.D. Wildman, R.J.M. Hague, Mater. Sci. Eng.: A 670 (2016) 264–274.
[53] A. Jung, S. Diebels, Adv. Eng. Mater. 21 (2019) 1900237.
[54] A. Aldoshan, S. Khanna, Mater. Sci. Eng.: A 689 (2017) 17–24.
[55] S.Y. Choy, C.-N. Sun, K.F. Leong, J. Wei, Mater. Des. 131 (2017) 112–120.
[56] B. Xie, Y. Fan, T. Mu, B. Deng, Mater. Sci. Eng.: A 708 (2017) 419–423.
[57] Y. Alvandi-Tabrizi, A. Rabiei, Procedia Mater. Sci. 4 (2014) 377–382.
[58] J.C. Qiao, Z.P. Xi, H.P. Tang, J.Y. Wang, J.L. Zhu, Mater. Trans. 49 (2008) 2919–2921.
[59] L. Zhang, S. Feih, S. Daynes, S. Chang, M.Y. Wang, J. Wei, W.F. Lu, Additive Manuf. 23 (2018) 505–515.
[60] C. Bonatti, D. Mohr, Acta Mater. 164 (2019) 301–321.
[61] S. Fan, T. Zhang, K. Yu, H. Fang, H. Xiong, Y. Dai, J. Ma, D. Jiang, H. Zhu, Trans. Nonferrous Metals Soc. China 27 (2017) 117–124.
[62] H. Gao, Y. Huang, W. Nix, J. Hutchinson, J. Mech. Phys. Solids 47 (1999) 1239–1263.
[63] L. Kubin, A. Mortensen, Scr. Mater. 48 (2003) 119–125.
[64] M. Calcagnotto, D. Ponge, E. Demir, D. Raabe, Mate. Sci. Eng.: A 527 (2010) 2738–2746.
[65] A.E. Jakus, S.L. Taylor, N.R. Geisendorfer, D.C. Dunand, R.N. Shah, Adv. Funct. Mater. 25 (2015) 6985–6995.